Korean J. Chem. Eng., 39(6), 1412-1423 (2022)
DOI: 10.1007/s11814-021-1047-2

pISSN: 0256-1115
eISSN: 1975-7220

Numerical simulation of thermal performance of bionic waste heat utilization equipment filled with nanofluids

Jianglin Tu, Cong Qi†, Liang Sun, Yuxing Wang, and Zhibo Tang

School of Low-carbon Energy and Power Engineering, China University of Mining and Technology, Xuzhou 221116, China
(*Received 13 September 2021 • Revised 16 November 2021 • Accepted 17 December 2021*)

Abstract−This paper, mainly through designing a reinforced structure from the perspective of bionics and substituting a new heat exchange working medium for the traditional working medium, attempted to figure out the thermal performance of the waste heat recovery device. By means of numerical method, the following five factors, namely the effects of Reynolds number (Re=1,300-1,800), the new heat transfer medium (CuO-H_2O nanofluids), the angular frequency of the bionic reinforced structure (ω=20 rad/s, ω=25 rad/s, ω=30 rad/s), the amplitude of the bionic reinforced structure (A=1 mm, A=2 mm, A=3 mm), and the phase shift of the bionic reinforced structure (α=0°, 90°, 180°) were probed so as to reveal their effects on the thermal performance of the waste heat recovery unit as well as the latent influencing mechanism. It was found that the improvement of the thermal transmission performance of the afterheat recovery unit synchronizes with the increase of angular frequency, amplitude and phase shift.

Keywords: Nanofluids, Bionic Structure, Waste Heat Utilization Equipment, Thermal Performance

INTRODUCTION

As the global economy grows, more and more attention is being paid to saving energy and protecting the environment [1,2]. Nonrenewable resources, such as oil and coal, are gradually decreasing. How to improve the energy efficiency and develop new energy sources (solar energy [3,4] and geothermal energy [5,6]), obviously, has become a hot topic in current researches.

With the development of industrial technology, industrial production has become the main way of energy consumption, in which waste heat resources account for about 70% of its fuel consumption [7]. Obviously, the secondary utilization of waste heat resources is an important way to improve energy utilization efficiency. How to improve the thermal performance of waste heat utilization devices has become a hot research topic [8]. As for the improvement of the thermal performance of waste heat devices, we can start from two aspects: adopting reinforced structure [9] and replacing traditional working medium with new working medium [10].

Appropriate reinforced structure can highly increase the energy transfer efficiency of a heat exchange system [11,12]. Qiu et al. [13] studied the influence of the number of heat exchange tubes on heat transfer efficiency in waste heat recovery by numerical simulation. Qi et al. [14] studied the influence of fin structure on the comprehensive cooling characteristics of a radiator through experiments. Pourmehran et al. [15] studied the thermal exchange property of the working medium in fin microchannels. Sheikholeslami et al. [16] studied how porous medium structure affects the thermal exchange performance of thermal exchange substance in the cavity. Li et al. [17] probed the impact of ties with disparate pitch ratio and height ratio on forced convection heat transfer characteristics in tubes. Qi et al. [18], aiming to enhance the cooling efficiency of electronic components, explored the thermal-hydraulic performance of foam metal and cylindrical reinforced structures.

Nanofluids are extensively utilized in diverse fields (heat exchangers [19], heat pipes [20], solar thermal collectors [21]) as a new heat transfer medium with uniform [22], stable [23] and high thermal conductivity [24]. Yan et al. [25] discussed the natural convection thermal transmission characteristics of CuO-H_2O nanofluid in the cavity, and found that adding copper oxide nanoparticles can increase Nusselt number and enhance heat transfer. Pourfattah and Mohebbi et al. [26,27], attempting to study the flow and heat exchange properties of nanofluids in microchannels, conducted research by numerical simulation, and found that nanoparticles can improve the comprehensive performance of working fluids. Sheremet et al. [28] applied alumina nanofluids to the cooling of electronic equipment, and analyzed the heat dissipation characteristics of electronic equipment by simulation. Sarafraz et al. [29] analyzed the thermal-hydraulic performance of gallium nanofluids with different mass fractions in solar thermal receivers. Selimefendigil et al. [30] researched into the natural convection thermal diffusion characteristics of carbon nanotube-water nanofluid in the cavity. Naphon et al. [31] employed a neural network to make clear the flow and heat transfer traits of nanofluid in radiator.

To sum up, many researchers have studied the influence of adopting strengthened structure and new heat exchange medium on heat exchange system in the fields of electronic component cooling and heat exchanger. Nevertheless, there are few researches on waste heat utilization devices. Therefore, on the basis of the finite volume method, we analyzed the influence of snake-shaped bionic enhanced surface structure and new heat transfer medium on the thermal performance of waste heat utilization device by simulation. The innovations of this paper mainly manifest in the follow-

†To whom correspondence should be addressed.
E-mail: qicong@cumt.edu.cn

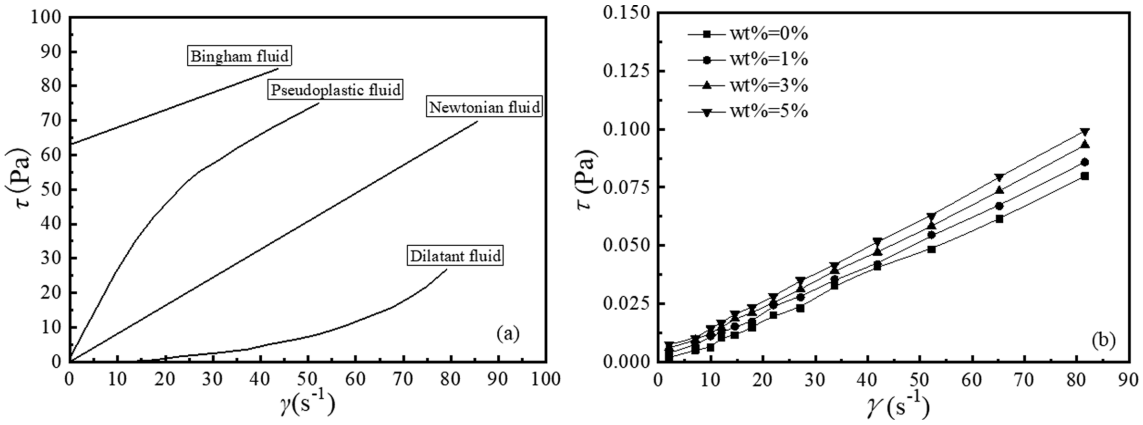

Fig. 1. Rheological curves of various fluids: (a) Newtonian fluid and non-Newtonian fluid [32], (b) CuO-H_2O nanofluids.

ing three aspects: first, the new heat exchange working medium (CuO-H_2O nanofluids) was selected and used for waste heat recovery device; secondly, a reinforced structure was abstracted from the perspective of bionics and applied to the waste heat recovery device; thirdly, the influence on the thermal performance of waste heat recovery devices exerted by different angular frequencies, amplitudes and phase shifts was analyzed by numerical methods.

THERMO-PHYSICAL PROPERTIES OF NANOFLUIDS

As an important inorganic material, copper oxide nanoparticles are widely used in catalysis, superconductivity, ceramics and other fields. They can be used as catalyst, catalyst carrier and electrode active material, and the copper oxide-water nanofluids have high thermal conductivity and good stability. Therefore, in this study, copper oxide-water nanofluid was used as heat exchange medium. Rheological curves of various fluids are shown in Fig. 1. Fig. 1(a) shows the rheological curves of Newtonian fluid and non-Newtonian fluid [32]. The rheological curve of the working medium used here is shown in Fig. 1(b). The relationship between shear rate and shear stress was found to be linear; therefore, the heat exchange medium used in this paper was Newtonian fluid.

The viscosity of nanofluids can be calculated according to Eq. (1) [33]:

$$\mu_{nf}=\mu_{bf}\frac{1+0.5\varphi}{(1-\varphi)^2} \tag{1}$$

where, μ_{nf}, μ_{bf} and φ denote viscosity of nanofluids, viscosity of base solution, volume fraction of particles contained in nanofluids, respectively.

When the volume fraction of nanoparticles is less than 5%, without considering the hydrodynamic interactions between the particles, the above equation can be simplified as follows Eq. (2):

$$\mu_{nf}=\mu_{bf}(1+2.5\varphi) \tag{2}$$

At this time, the density and specific heat formulas of nanofluids will be conveyed as follows Eq. (3) and Eq. (4) [34]:

$$\rho_{nf}=(1-\varphi)\rho_f+\varphi\rho_p \tag{3}$$

$$(c_p)_{nf}=(1-\varphi)(c_p)_f+(c_p)_p \tag{4}$$

where, ρ_{nf} is density of nanofluids, ρ_f is the density of base solution, ρ_p is the density of nanoparticles, $(c_p)_{nf}$ is the specific heat at constant pressure of nanofluids and $(c_p)_p$ is the specific heat at constant pressure of nanoparticles.

The calculation formula for the thermal conductivity of nanofluids is shown below, Eq. (5) [35]:

$$k_{co}=\frac{(k_{p2}+2k_{p1})-2\varphi(k_{p1}-k_{p2})}{(k_{p2}+2k_{p1})+\varphi(k_{p1}-k_{p2})} \tag{5}$$

where, k_{co} is the thermal conductivity of CuO nanofluids, k_{p1} is the thermal conductivity of water, k_{p2} is the thermal conductivity of CuO, and φ represents the volume fraction of nanofluids.

The Reynolds number of the working fluid is calculated according to Eq. (6) and Eq. (7):

$$Re=\frac{\rho_{nf}uD}{\mu_{nf}} \tag{6}$$

where

$$D=\frac{4Ac}{L} \tag{7}$$

In this paper, CuO-H_2O nanofluids was studied. The concentration of CuO-H_2O nanofluids is distinguished by mass fraction method. The density, thermal conductivity and specific heat of nanofluids with mass fraction of 1%, 3% and 5% are different, so the concentration of nanofluids can be distinguished by modifying physical parameters when setting simulation conditions. The thermophysical parameters of base fluid (water) and copper oxide nanoparticles are made clear in Table 1. The thermophysical parameters of CuO-H_2O nanofluids are demonstrated in Table 2. The mass fraction of nanofluids is 0-0.5 wt%, because when the mass fraction of nanofluids exceeds 1%, the increase of nanofluid mass frac-

Table 1. Physical parameters of each phase

Physical parameters	Base fluid (water)	Nanoparticle (CuO)
ρ/(kg·m^{-3})	997.1	6,500
c_p/(J·kg^{-1}K^{-1})	4,179	540
μ/(m^2·s^{-1})	0.001004	--
k/(W·m^{-1}K^{-1})	0.614	18

Table 2. Physical parameters of nanofluids

Physical parameters	ρ/(kg·m^{-3})	c_p/(J·kg^{-1}K^{-1})	k/(W·m^{-1}K^{-1})	μ/(m^2·s^{-1})
CuO-H_2O (φ=0.01)	1,052.129	3,954.1844	0.6297827	0.0010295
CuO-H_2O (φ=0.03)	1,162.187	3,568.4227	0.6642842	0.0010834
CuO-H_2O (φ=0.05)	1,272.245	3,249.4031	0.7000929	0.0011413

tion will not only improve the thermal performance of working fluid, but also adversely affect the stability of nanofluids, resulting in waste of resources. Therefore, we chose a lower mass fraction for research.

MODEL CONFIRMATION

1. Physical Model

Herein, waste heat utilization equipment with bionic strengthening structure was studied, with its structure plotted in Fig. 2. The waste heat utilization equipment consists of a bottom thermoelectric plate and an upper heat exchanger.

Nanofluids absorb afterheat, which flows into the cavity of the heat exchanger and transfers the heat to the thermoelectric plate through the bionic enhanced surface. Specific parameters of the bionics-inspired snake-shaped bionic channel structure are shown in Table 3.

2. Governing Equations

To save resources, numerical simulation settles the flow and heat transfer problems by solving three major equations. The maximum fluid Reynolds number studied in this paper is 1,800, so the corresponding conservation equations need to be solved under laminar flow conditions. At present, there are two main methods for numerical simulation of nanofluids: single-phase simulation and two-phase simulation. The single-phase simulation method regards the base fluid and nanoparticles in nanofluids as a single fluid with uniform and stable distribution, and describes nanofluids with the original governing equation of single fluid. The nanofluids prepared in this paper have good dispersibility and stability, and the CuO nanoparticles are very small. Therefore, it can be approximately consid-

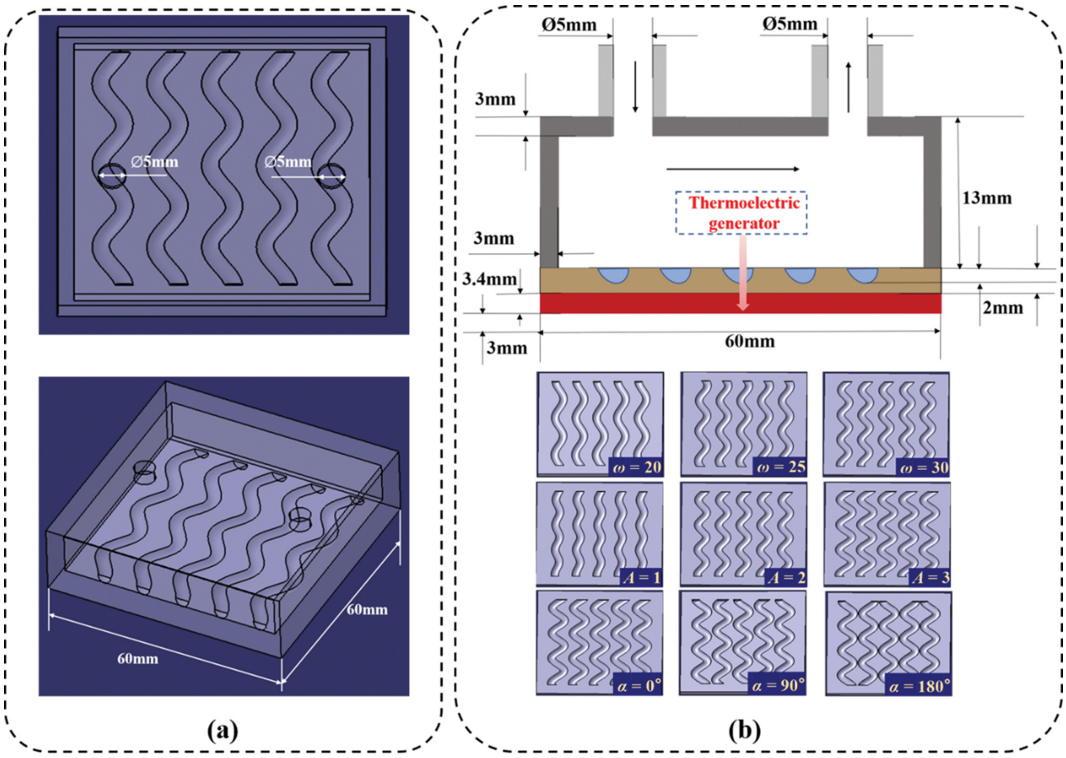

Fig. 2. Geometric model: (a) Overall structure, (b) Partial enlarged detail.

Table 3. Parameters of bionic wave channel structures with different shapes

Parameter	Variable value			Remarks
Angular frequency (ω)	20 rad/s	25 rad/s	30 rad/s	α=0°, A=2 mm
Amplitude (A)	1 mm	2 mm	3 mm	α=0°, ω=30 rad/s
Phase shift (α)	0°	90°	180°	A=3 mm, ω=30 rad/s

ered that the behavior of nanoparticles is similar to that of fluids [36]. Single-phase numerical simulation can ensure the same accuracy, and the calculation speed is faster. So, this paper adopted the method of single-phase simulation to study nanofluids.

To simplify the calculation process, the following assumptions related to the flow and heat transfer process of waste heat utilization equipment were made: (1) The physical parameters of nanofluids are constant values, independent of temperature and pressure; (2) The heat exchange medium is regarded as a Newtonian fluid; (3) The thermoelectric plate is regarded as an isotropic object, ignoring the internal structure of the thermoelectric plate; and (4) Contact thermal resistance is ignored between thermoelectric plate and heat exchanger.

In the process of numerical analysis, the governing equations in regard to the flow and thermal transmission of working medium in afterheat utilization equipment are as follows [37]:

Continuity equation is shown in Eq. (8):

$$\nabla \cdot \vec{U} = 0 \tag{8}$$

Momentum equation is shown in Eq. (9):

$$\rho_f(\vec{U} \cdot \nabla \vec{U}) = -\nabla P + \nabla(\mu_f \nabla \vec{U}) \tag{9}$$

Energy equation in Eq. (10):

$$\rho_f c_p(\vec{U} \cdot \nabla T_f) = \nabla(\lambda_f \nabla T_f) + \Phi \tag{10}$$

where ρ_f, c_p, f, λ_f, μ_f represent working fluid density, specific heat capacity, thermal conductivity and dynamic viscosity, respectively. Φ is the viscous dissipation term.

3. Numerical Calculation Method and Model Verification

3-1. Numerical Computation Method and Boundary Conditions

First, the 3D physical model is established by CATIA software, then the mesh is divided by ICEM software, and the bionic sur-

Table 4. Grid independence verification results

Hot side temperature	Grid number	748,113	995,670	1,301,671	1,678,543	Literature [38]
	Calculation results	42.07	41.68	41.57	41.48	41.26
	Error	1.96%	1.02%	0.75%	0.53%	
Nusselt number	Grid number	748,113	995,670	1,301,671	1,678,543	Literature [38]
	Calculation results	7.76	7.87	7.96	7.99	8.02
	Error	3.24%	1.91%	0.75%	0.37%	

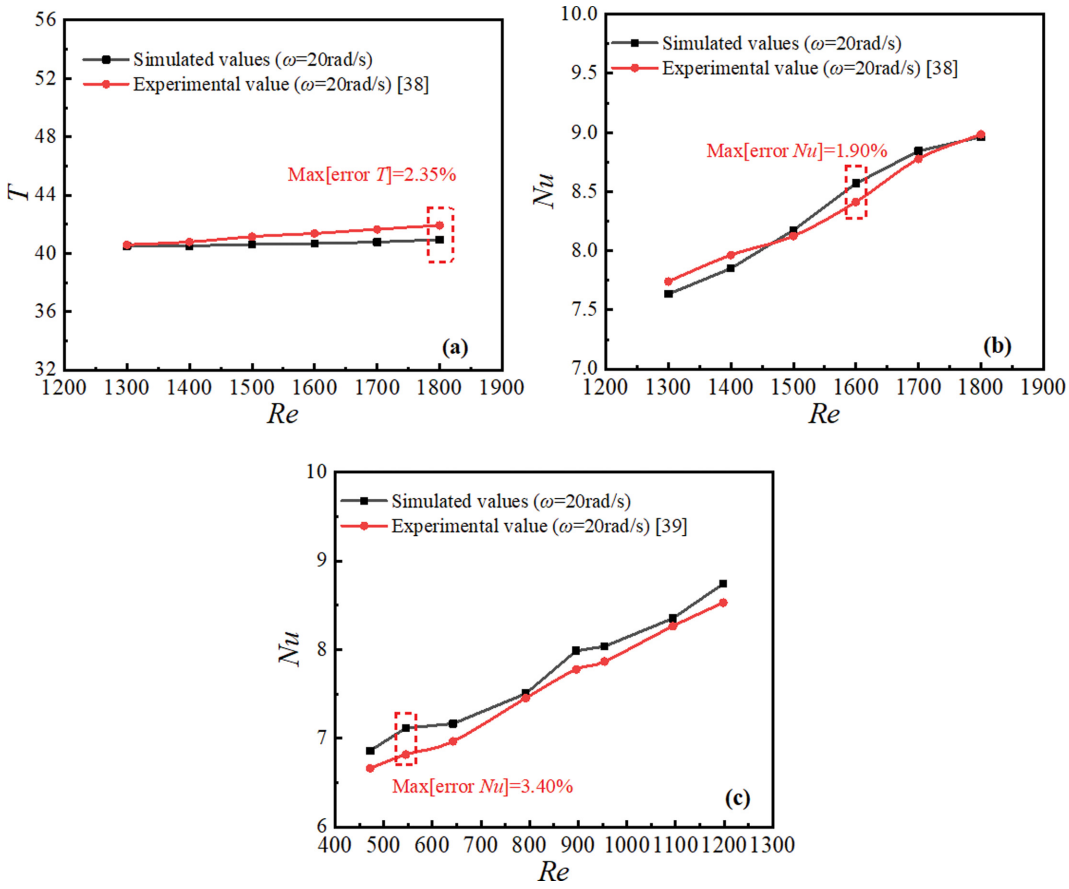

Fig. 3. Verification of hot side temperature of thermoelectric plate and Nusselt number: (a) T, (b) Nu at high Re, (c) Nu at low Re.

face is encrypted. Finally, Fluent software is used to solve the problem. The laminar flow model was used to analyze the flow and heat transfer characteristics of waste heat utilization equipment. The governing equations with relevant boundary conditions were discretized by finite volume method. The continuity, momentum and energy equations were discretized by the second-order upwind scheme. In the solution setting, SIMPLE algorithm was adopted, and the convergence accuracy was 10^{-6}.

The boundary conditions for numerical calculation are set as follows: (1) The inlet of the cavity is a velocity inlet, and the temperature remains unchanged when the working medium enters the cavity; (2) The outlet of the cavity is a pressure outlet; (3) According to the experimental results, the boundary of the corresponding temperature is set at the cold end of the thermoelectric plate; and (4) There is no velocity slip at the interface between fluid and cavity wall.

3-2. Grid Independence Verification

The number of grids will exert an influence on the accuracy and calculation speed of numerical simulation, so it is necessary to select the appropriate number of grids. Taking the model with angular frequency of 20 rad/s as an example, the grid independence was verified. The thermal performance of afterheat utilization equipment was numerically analyzed with four grid numbers of 748,113, 995,670, 1,301,671 and 1,678,543, respectively, and the inlet velocity was 0.49 m/s. The verification results of grid independence are shown in Table 4. When the number of grids was 1,301,671, the temperature error at the hot side of thermoelectric plate was 0.75%, and the Nusselt number error was 0.75%, which not only can ensure the accuracy of calculation results, but also save calculation resources. Therefore, the number of grids in the calculation area was determined to be 1,301,671. In this paper, the same method was used to verify grid independence for other working conditions.

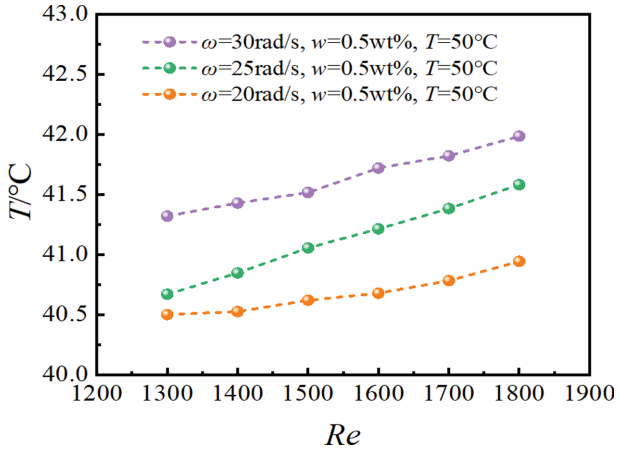

Fig. 4. Temperature at hot end of thermoelectric plate under different angular frequencies.

3-3. Reliability Verification of Numerical Model

To ensure the reliability of the calculation model, we still take the model with an angular frequency of 20 rad/s as an example, comparing the numerical calculation results with those of the literature [38]. The results are shown in Fig. 3(a) and (b). In the range of Reynolds numbers from 1,300 to 1,800, the maximum errors of the hot side temperature of thermoelectric plate and Nusselt number are 2.35% and 1.90% respectively. In addition, the numerical model was applied to analyze the heat transfer characteristics of heat exchangers with similar structures [39] as this paper. The comparison between numerical results and literature values [39] is shown in Fig. 3(c). It is found that the maximum error between the experi-

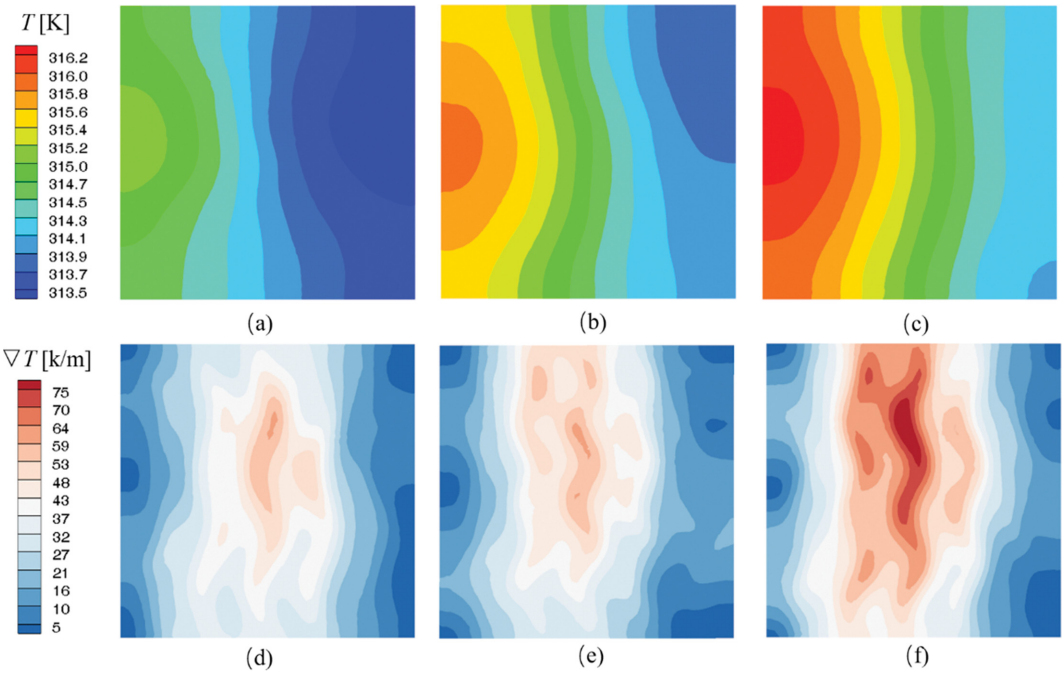

Fig. 5. The temperature and temperature gradient distribution nephogram for Re=1,800: (a) ω=20 rad/s, (b) ω=25 rad/s, (c) ω=30 rad/s, (d) ω=20 rad/s, (e) ω=25 rad/s, (f) ω=30 rad/s.

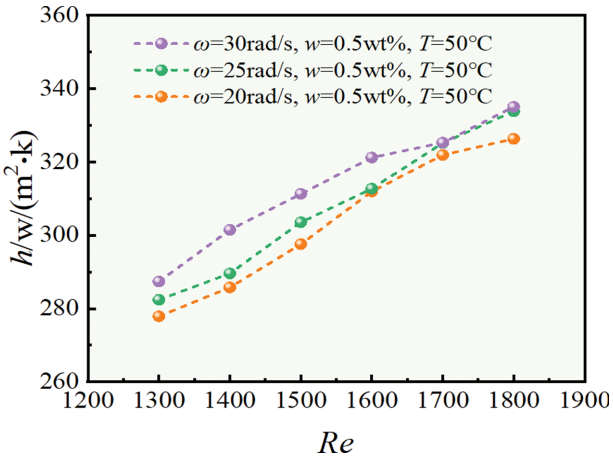

Fig. 6. Convective heat transfer coefficient of nanofluids under different angular frequencies.

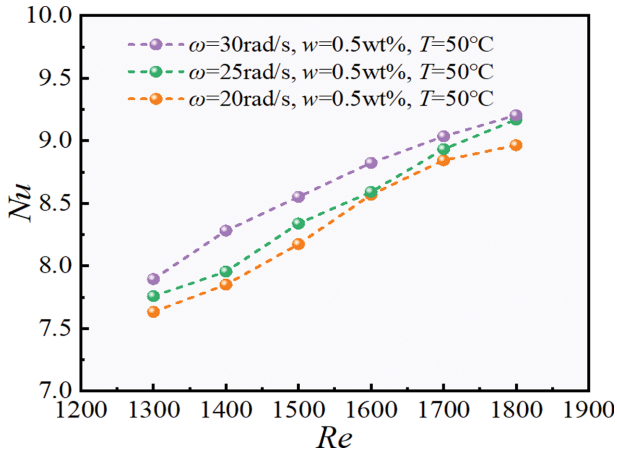

Fig. 7. Nusselt numbers of nanofluids under different angular frequencies.

mental value and the simulation result was 3.40%. To sum up, the numerical model can control the error within a reasonable range. Therefore, the numerical model in this paper is reliable.

RESULTS AND DISCUSSION

1. Influence of Angular Frequency

In our previous research [38], various working conditions were studied in detail through experiments. In this paper, numerical simulation was carried out for waste heat temperature of 50 °C and nanofluids mass fraction of 0.5%. At first, the influence of different angular frequencies (ω=20 rad/s, ω=25 rad/s, ω=30 rad/s) on waste heat utilization equipment was studied by numerical analysis. Fig. 4 quantitatively analyzes the change of temperature at the hot side of thermoelectric plate with Reynolds number. The conclusion is that the increment of angular frequency facilitates the improvement of the heat transfer of waste heat utilization equipment.

The hot-end temperature with a radian frequency of 30 rad/s is 1.60% higher than that of 25 rad/s, and the hot-end temperature with an angular frequency of 25 rad/s is 1.56% higher than that of 20 rad/s. The reason for this result is that the wave number under the same surface area increases with angular frequency, which intensifies the disturbance of the working fluid caused by the bionic structure, decreases the thermal resistance of the bounding layer, thus promoting thermal transmission. Fig. 5 visually shows the nephogram of temperature and temperature gradient distribution at the hot side of thermoelectric plate when Reynolds number is 1,800. Obviously, increasing the radian frequency is conducive to boosting the heat transfer of afterheat utilization equipment, while the temperature gradient in the middle area of the hot side of the thermoelectric plate increases slightly.

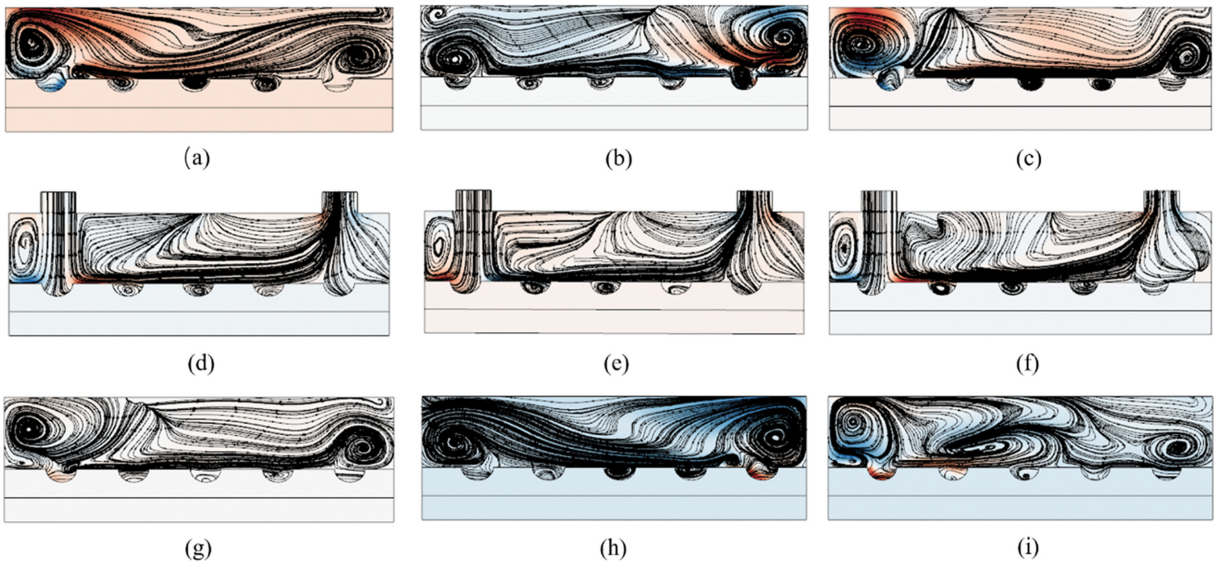

Fig. 8. Streamline distribution at different sections for Re=1,800: (a) ω=20 rad/s, y=−10 mm, (b) ω=25 rad/s, y=−10 mm, (c) ω=30 rad/s, y=−10 mm, (d) ω=20 rad/s, y=0 mm, (e) ω=25 rad/s, y=0 mm, (f) ω=30 rad/s, y=0 mm, (g) ω=20 rad/s, y=10 mm, (h) ω=25 rad/s, y=10 mm, (i) ω=30 rad/s, y=10 mm.

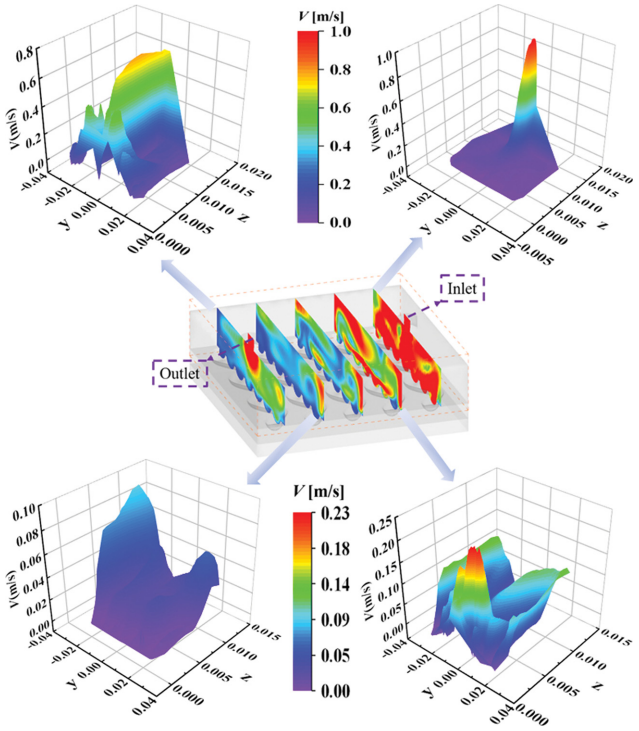

Fig. 9. Velocity distribution at different sections for ω=30 rad/s.

In addition to investigating the hot side temperature of the thermoelectric plate, the heat transfer of CuO-H_2O nanofluids in the heat exchanger cavity is also discussed. Fig. 6 and Fig. 7, respectively, show the variation of convective heat transfer coefficient and

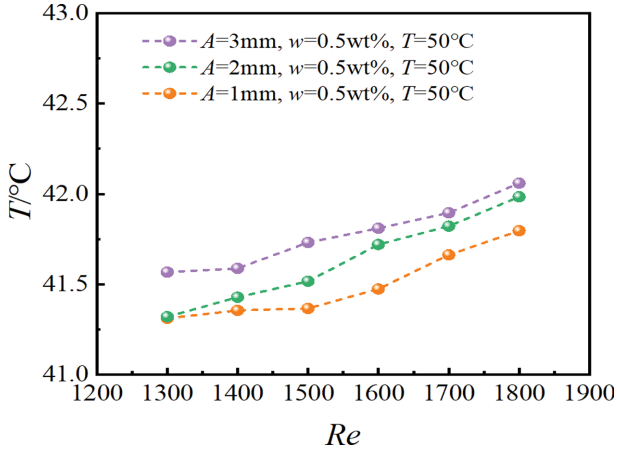

Fig. 10. Temperature at hot end of thermoelectric plate under different amplitudes.

Nusselt number with Reynolds number. It can be found that with angular frequency increasing, so does the convective heat transfer coefficient and Nusselt number, which further reveals the enhancement of the heat transfer performance of waste heat utilization equipment. Moreover, the Nusselt number with a radian frequency of 30 rad/s is 4.10% higher than that of 25 rad/s, and the Nusselt number with a radian frequency of 25 rad/s is 2.29% higher than that of 20 rad/s. The reason is the same as Fig. 4.

Finally, the influencing mechanism of bionic strengthening structure acting on the performance of afterheat recovery equipment was analyzed from the perspective of flow field and velocity field. Fig. 8 shows the streamline distribution at different sections in the heat

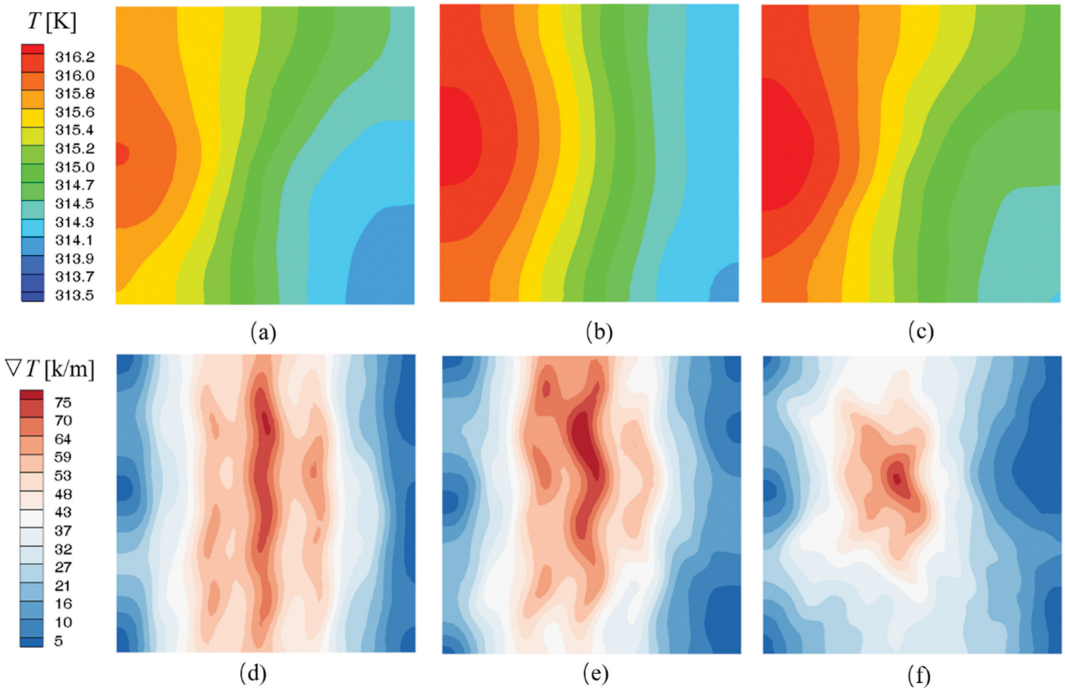

Fig. 11. The temperature and temperature gradient distribution nephogram for Re=1,800: (a) A=1 mm, (b) A=2 mm, (c) A=3 mm, (d) A=1 mm, (e) A=2 mm, (f) A=3 mm.

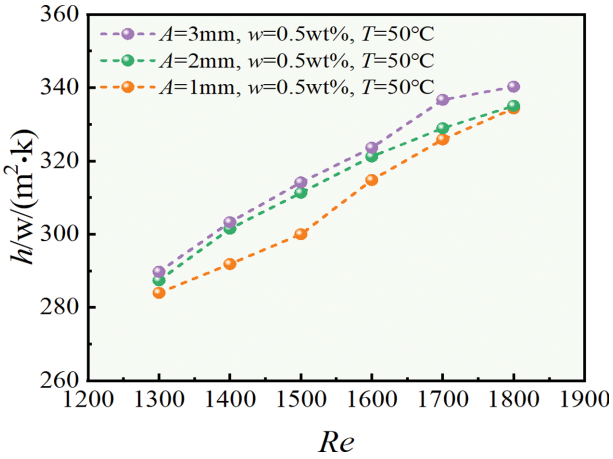

Fig. 12. Convective heat transfer coefficient of nanofluids under different amplitudes.

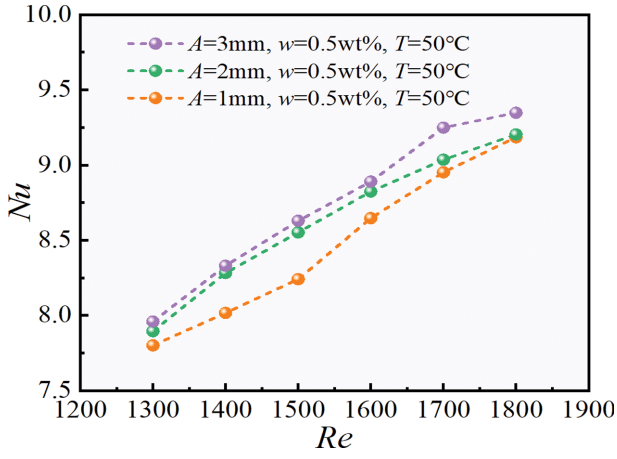

Fig. 13. Nusselt numbers of nanofluids under different amplitudes.

exchanger cavity. According to Fig. 8, as angular frequency increases, so do the turbulence degree of fluid flow and the number of vortices, thus contributing to the enhancement of the heat transfer, which also intuitively explains why the bionic enhanced structure can increase the heat transfer.

To analyze the temperature gradient distribution, Fig. 9 shows the velocity distribution nephogram in the heat exchanger cavity with angular frequency of 30 rad/s and Reynolds number of 1,800. It can be seen that from the fluid inlet to the outlet direction, the velocity of the fluid is obviously decreasing, indicating that the velocity gradient along the fluid flow direction is larger, which increases the unevenness of fluid flow and finally leads to nonuniform temperature at the hot side of the thermoelectric plate, which is an unfavorable factor for improving the efficiency of the thermoelectric plate.

2. Influence of Amplitude

The research in the previous section [38] found that the waste heat utilization equipment with an angular frequency of 30 rad/s has the best heat transfer performance, so the fixed angular frequency in this section is 30 rad/s, and the influence of amplitude on thermal transmission performance of waste heat utilization equipment is further studied. It can be found, by interpreting Fig. 10, that the thermal transmission performance of afterheat recovery equipment increases with amplitude. The temperature at the hot side of the thermoelectric plate with amplitude of 3 mm is 0.64% higher than that of thermoelectric plate with amplitude of 2 mm, which is 0.59% higher than that of thermoelectric plate with amplitude of 1 mm.

This is because with the increment of amplitude, under the condition of the same wave number, the area proportion of bionic reinforced structure increases, the turbulence degree of fluid flow increases, and finally the heat transfer is enhanced. Fig. 11 visually

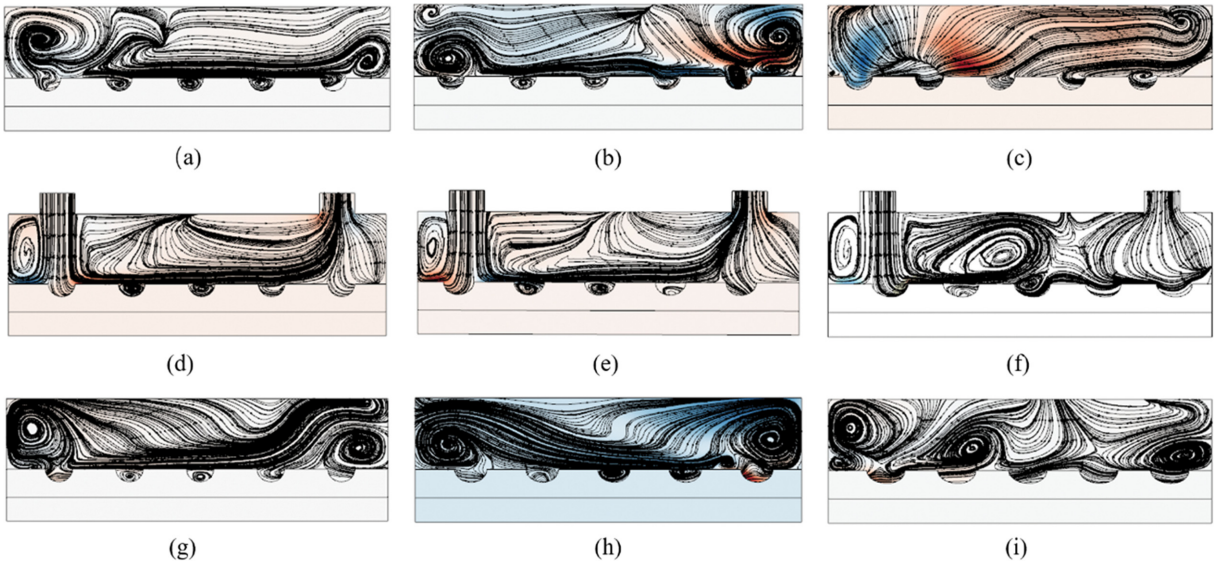

Fig. 14. Streamline distribution at different sections for Re=1,800: (a) A=1 mm, y=−10 mm, (b) A=2 mm, y=−10 mm, (c) A=3 mm, y=−10 mm, (d) A=1 mm, y=0 mm, (e) A=2 mm, y=0 mm, (f) A=3 mm, y=0 mm, (g) A=1 mm, y=10 mm, (h) A=2 mm, y=10 mm, (i) A=3 mm, y=10 mm.

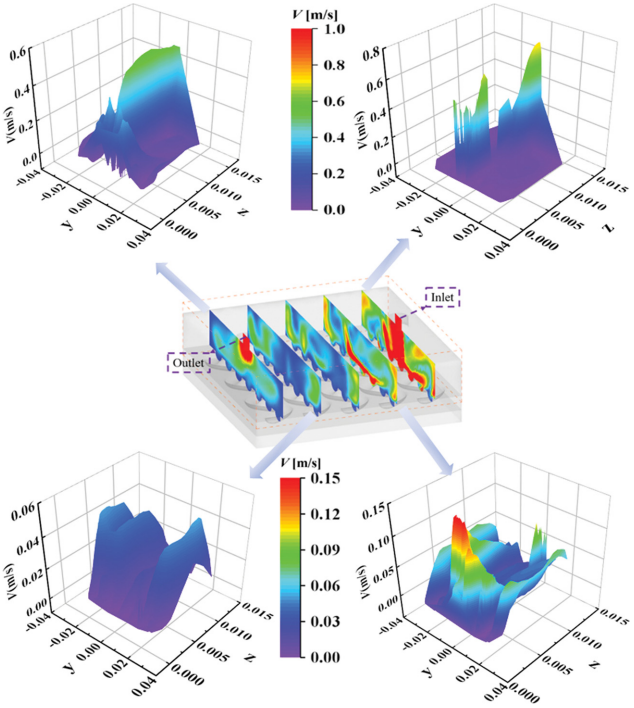

Fig. 15. Velocity distribution at different sections for A=3 mm.

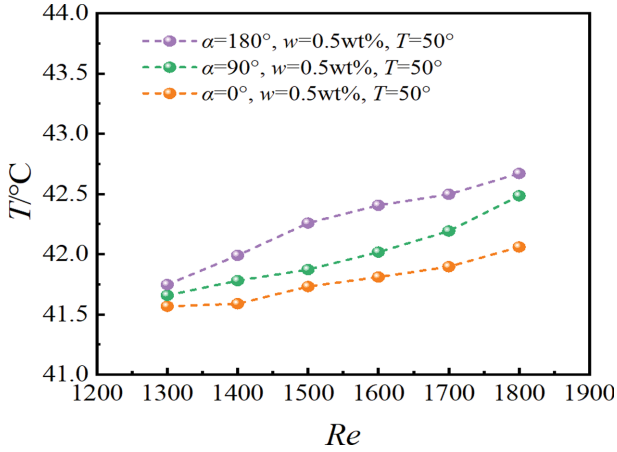

Fig. 16. Temperature at hot end of thermoelectric plate under different phase shifts.

shows the nephogram of temperature and temperature gradient distribution at the hot side of the thermoelectric plate when Reynolds number is 1,800. It can be clearly seen that increasing the amplitude can raise the temperature at the hot end of the thermoelectric plate, so will the temperature gradient accordingly, which is beneficial for improving the power generation efficiency of the thermoelectric chip.

To quantify the thermal transmission performance of afterheat utilization equipment, Fig. 12 and Fig. 13, respectively, show the variation laws of convective thermal transmission coefficient and Nusselt number with Reynolds number. It is obvious that both convective thermal transmission coefficient and Nusselt number simultaneously increase with amplitude. The Nusselt number with amplitude of 3 mm is 2.35% higher than that with amplitude of 2 mm, and the Nusselt number with amplitude of 2 mm is 3.77% higher than that with amplitude of 1 mm. The reason is the same as Fig. 10.

Finally, the influencing mechanism of bionic strengthening struc-

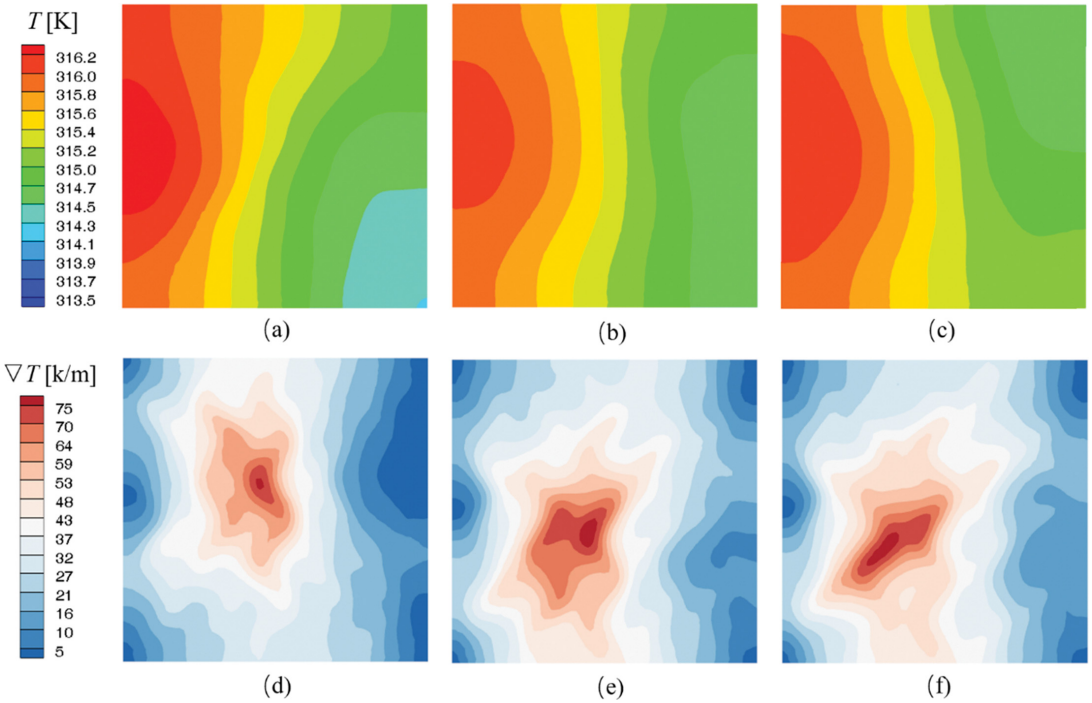

Fig. 17. The temperature and temperature gradient distribution nephogram for Re=1,800: (a) α=0°, (b) α=90°, (c) α=180°, (d) α=0°, (e) α=90°, (f) α=180°.

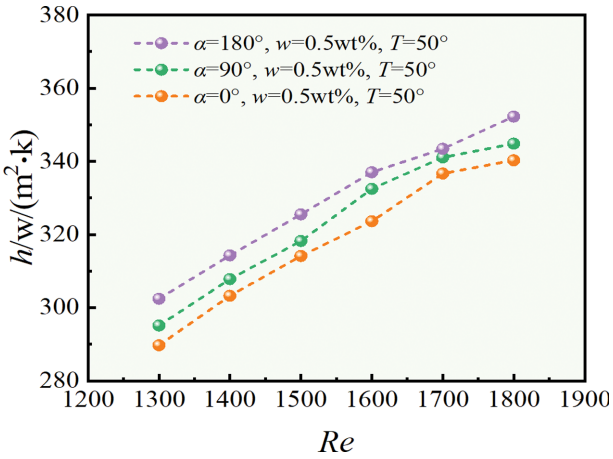

Fig. 18. Convective heat transfer coefficient of nanofluids under different phase shifts.

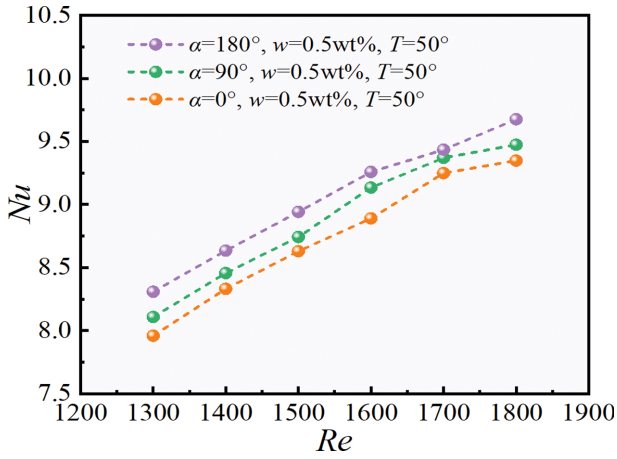

Fig. 19. Nusselt numbers of nanofluids under different phase shifts.

ture acting on the performance of afterheat recovery equipment was analyzed from the perspective of flow and velocity field. Fig. 14 shows the streamline distribution at different cross-sections in the heat exchanger cavity. From Fig. 14 we can clearly see the reason why increasing the amplitude can enhance the thermal transmission: the increase of the amplitude enhances the fluid turbulence and the number of vortices, which ultimately boosts heat transfer.

Fig. 15 shows a cloud diagram of velocity distribution in the heat exchanger cavity with the amplitude of 3 mm and Reynolds number of 1,800. Compared with Fig. 9, it can be found that in the fluid flow direction, the fluid velocity changes more smoothly and the fluid velocity distribution is more uniform, indicating that increasing the amplitude not only can improve the temperature at the hot side of the thermoelectric plate, but also make the temperature distribution at the hot side more uniform, which is greatly conducive to the improvement of the thermoelectric conversion efficiency of waste heat utilization equipment.

3. Influence of Phase Shift

The previous study [38] found that the best thermal transmission performance of the afterheat utilization equipment falls into the condition of an angular frequency of 30 rad/s and an amplitude of 3 mm, so in the next study the influence of phase shift on the waste heat utilization equipment was further studied by fixing the angular frequency of 30 rad/s and amplitude of 3 mm. By analyzing Fig. 16, it can be found that the temperature at the hot end of the thermoelectric plate increases with phase shift. The hot end temperature with a phase shift of 180° is 0.93% higher than that with a phase shift of 90°, and the hot end temperature with a phase shift of 90° is 1.01% higher than that with a phase shift of 0°.

Increasing the phase-shift angle gives rise to an increase of the temperature at the hot end of the thermoelectric plate, because the increase in phase shift angle will intensify the turbulence of the

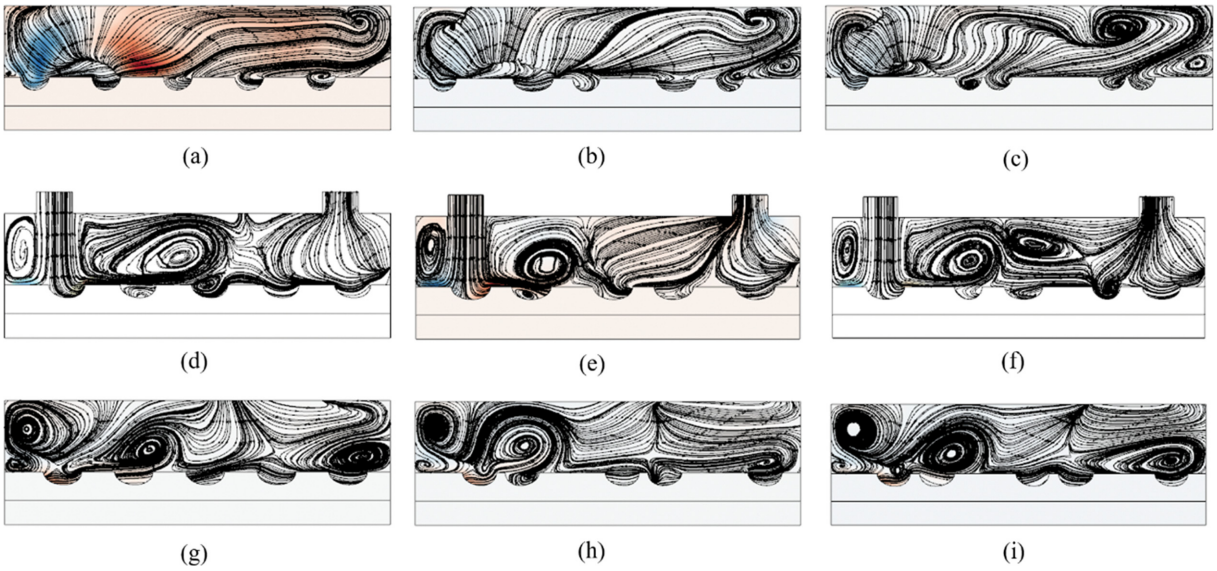

Fig. 20. Streamline distribution at different sections for Re=1,800: (a) α=0°, y=−10 mm, (b) α=90°, y=−10 mm, (c) α=180°, y=−10 mm, (d) α=0°, y=0 mm, (e) α=90°, y=0 mm, (f) α=180°, y=0 mm, (g) α=0°, y=10 mm, (h) α=90°, y=10 mm, (i) α=180°, y=10 mm.

fluid, augment the number of vortices, destroy the laminar boundary layer, thus enhancing the heat transfer in the end. Fig. 17 visually shows the nephogram of temperature and temperature gradient distribution at the hot side of the thermoelectric plate when Reynolds number is 1,800. It intuitively illustrates that the increase of the phase shift angle can raise the temperature of the hot side of the thermoelectric plate, while the temperature gradient distribution does not change significantly. This shows that while increasing the thermal transmission performance, it can also ensure the uniformity of the temperature distribution, which is helpful for improving power generation.

To quantify the heat transfer performance of waste heat utilization equipment, Fig. 18 and Fig. 19, respectively, show the variation laws of convective heat transfer coefficient and Nusselt number with Reynolds number. It is evident that both convective heat transfer coefficient and Nusselt number increase with phase shift simultaneously. The Nusselt number with 180° phase shift is 2.47% higher than that with 90° phase shift, and the Nusselt number with 90° phase shift is 2.74% higher than that with 0° phase shift. The reason is the same as Fig. 16.

Finally, the influencing mechanism of bionic strengthening structure acting on the performance of afterheat utilization equipment was analyzed from the angle of flow field and velocity field. Fig. 20 shows the streamline distribution at different cross-sections in the heat exchanger cavity. It is found that the increase of the phase shift angle enhances the turbulence degree and the number of vortices, and finally facilitates the heat transfer.

Fig. 21 shows the nephogram of velocity distribution in the heat exchanger cavity with phase shift angle of 180° and Reynolds number of 1,800. It can be found that the velocity distribution in Fig. 21 is slightly more uniform than that in Fig. 15, which indicates that the heat transfer performance of waste heat utilization equipment can be continuously improved while ensuring the uniformity of temperature distribution, so as to maximize the thermoelectric performance of afterheat recovery equipment.

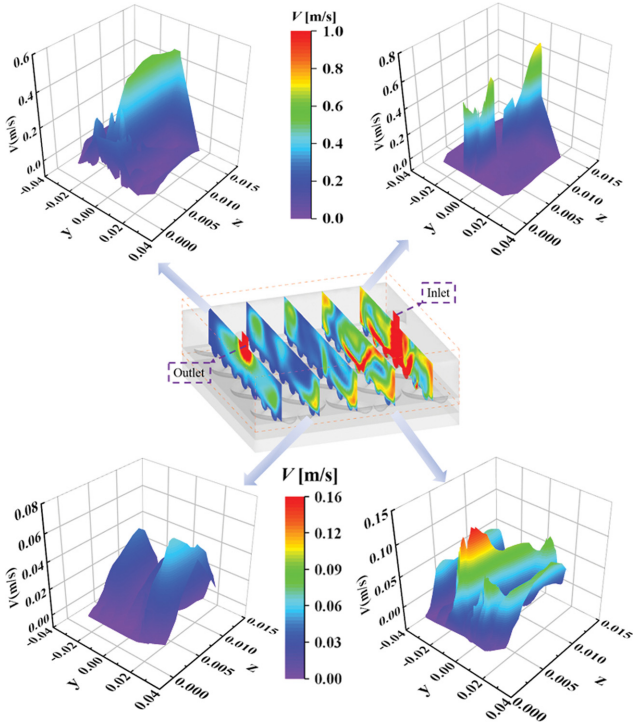

Fig. 21. Velocity distribution at different sections for α=180°.

CONCLUSIONS

Numerical simulation was applied to determine the influence of different bionic strengthening structures on the performance of afterheat recovery equipment, in the meantime, with the analysis of the influencing mechanism. The main research conclusions are as follows:

(1) The improvement of heat transfer performance of afterheat recovery equipment synchronizes with the increase of radian frequency, amplitude and phase shift. Increasing radian frequency, amplitude and phase shift can intensify the turbulence degree of fluid, enhance the number of vortices, cause more intense interference to fluid flow, and finally promote heat transfer.

(2) For bionic structures with different angular frequencies, the waste heat utilization device with ω=30 rad/s (α=0°, A=2 mm) has the best thermal performance. Compared with ω=20 rad/s, the hot end temperature and Nusselt number have increased by 2.56% and 5.49%, respectively.

(3) For bionic structures with different amplitudes, the thermal performance of the waste heat utilization device with A=3 mm (α=0°, ω=30 rad/s) is the best. Compared with A=1 mm, the hot end temperature and Nusselt number are increased by 0.88% and 4.72%, respectively.

(4) For bionic structures with different phase shifts, the waste heat utilization device with α=180° (A=3 mm, ω=30 rad/s) has the best thermal performance. Compared with α=0°, the hot end temperature and Nusselt number increased by 1.45% and 4.39% respectively.

The influence of bionic reinforced structure on the thermal performance of waste heat utilization device was analyzed by numerical simulation. In future work, the thermoelectric coupling characteristics of waste heat utilization device will be deeply studied by numerical simulation.

ACKNOWLEDGEMENTS

This work is financially supported by National Natural Science Foundation of China (Grant No. 51606214) and Natural Science Foundation of Jiangsu Province, China (Grant No. BK20181359).

NOMENCLATURE

A : amplitude [mm]
A_c : cross-sectional area [m^2]
c_p : specific heat [J $kg^{-1}K^{-1}$]
$(c_p)_{nf}$: specific heat at constant pressure of nanofluids [J $kg^{-1}K^{-1}$]
$(c_p)_p$: specific heat at constant pressure of nanoparticles [J $kg^{-1}K^{-1}$]
k : heat conductivity coefficient [W $m^{-1}K^{-1}$]
L : length [m]
u : velocity of nanofluids [m·s^{-1}]

Greek Symbols

α : phase shift [°]
ρ : density of nanofluids [kg·m^{-3}]
ρ_f : density of base fluid [kg·m^{-3}]
ρ_p : density of nanoparticles [kg·m^{-3}]
μ : viscosity [m^{2}s^{-1}]
φ : nanoparticle volume fraction [%]
ω : angular frequency [rad/s]

Subscripts

bf : base fluid
nf : nanofluids
np : nanoparticle

REFERENCES

1. F. Selimefendigil and H. F. Öztop, *Int. J. Mech. Sci.*, **194**, 106210 (2021).
2. X. Wang, X. Gao, K. Bao, C. Hua, X. Han and G. Chen, *Int. J. Therm. Sci.*, **28**, 246 (2019).
3. H. Jin, G. Lin, Y. Guo, L. Bai and D. Wen, *Renew. Energ*, **145**, 2337 (2020).
4. Z. Li, F. Selimefendigil, M. Sheikholeslami, A. Shafee and M. Alghamdi, *Microsyst. Technol.*, **26**(2), 333 (2020).
5. M. Afrand, A. Shahsavar, P. T. Sardari, K. Sopian and H. Salehipour, *Sol. Energy*, **188**, 83 (2019).
6. F. Selimefendigil, F. Bayrak and H. F. Oztop, *Renew. Energ.*, **125**, 193 (2018).
7. F. Selimefendigil and H. F. Öztop, *Renew. Energ.*, **162**, 1076 (2020).
8. S. Khanmohammadi, M. Saadat-Targhi, F. W. Ahmed and M. Afrand, *Int. J. Hydrogen Energ*, **45**, 6934 (2020).
9. M. Sheikholeslami, A. Arabkoohsar and M. Jafaryar, *J. Energy Resour. Technol*, **142**(11), 1 (2020).
10. X. Wang, X. Yan, N. Gao and G. Chen, *J. Therm. Sci.*, **29**(6), 1504 (2020).
11. C. Qi , T. Luo, M. Liu, F. Fan and Y. Yan, *Energy Convers. Manage.*, **197**, 111877 (2019).
12. F. Selimefendigil and H. F. Öztop, *J. Cleaner Prod.*, **279**, 123426 (2021).
13. L. Qiu, D. Sang, Y. Feng, H. Huang and X. Zhang, *Chem. Eng. Process.*, **151**, 107915 (2020).
14. C. Qi, K. Li, C. Li, B. Shang and Y. Yan, *Int. Commun. Heat Mass Transf.*, **114**, 104589 (2020).
15. O. Pourmehran, M. Rahimi-Gorji, M. Hatami, S. Sahebi and G. Domairry, *J. Taiwan Inst. Chem. Eng.*, **55**, 49 (2015).
16. M. Sheikholeslami, M. M. Bhatti, A. Shafee and Z. Li, *Comput. Thermal. Scien.*, **11**(5), 475 (2019).
17. M. Sheikholeslami, M. Jafaryar, S. Saleem, Z. Li, A. Shafee and Y. Jiang, *Int. J. Heat Mass Transf.*, **126**, 156 (2018).
18. C. Qi, T. Chen, J. Tu and Y. Wang, *Korean J. Chem. Eng.*, **37**(12), 2104 (2020).
19. M. Izadi and S. Naderi, *J. Mech. Eng.*, **49**(4), 9 (2019).
20. X. Wang, Y. Yan, X. Meng and G. Chen, *Appl. Therm. Eng.*, **157**, 113761 (2019).
21. F. Selimefendigil and H. F. Öztop, *Int. J. Heat Mass Transfer*, **178**, 121623 (2021).
22. X. Wang, E. Wright, N. Gao and Y. Lin, *Int. J. Therm. Sci.*, **1383**, 1 (2020).
23. Q. Nguyen, S. N. Sedeh, D. Toghraie, R. Kalbasi and A. Karimipour, *J. Braz. Soc. Mech. Sci. Eng.*, **42**(9), 1 (2020).
24. M. Ghaneifar, A. Raisi, H. M. Ali and P. Talebizadehsardari, *J. Therm. Anal. Calorim.*, **143**(3), 2761 (2021).
25. S. R. Yan, R. Kalbasi, D. Toghraie, X. X. Tian, Q. Nguyen and A. Karimipour, *Math. Meth. Appl. Sci.*, **46**, 6576 (2020).
26. F. Pourfattah, A. A. A. Arani, M. R. Babaie, H. M. Nguyen and A. Asadi, *Int. J. Heat Mass Transfer* **143**, 118518 (2019).
27. H. Sajjadi, A. A. Delouei, M. Izadi and R. Mohebbi, *Int. J. Heat Mass Transfer*, **132**, 1087 (2019).
28. M. A. Sheremet and M. M. Rashidi, *Alex. Eng. J.*, **60**(3), 2769 (2021).
29. M. Sarafraz and M. Arjomandi, *Int. Commun. Heat Mass Transf.*, **94**, 39 (2018).
30. F. Selimefendigil and H. F. Öztop, *Int. J. Heat Mass Transfer*, **129**, 265 (2019).
31. P. Naphon, S. Wiriyasart, T. Arisariyawong and L. Nakharintr, *Int. J. Heat Mass Transfer*, **131**, 329 (2019).
32. C. Qi, K. Li and C. Li, *CIESC J.*, **72**(4), 2006 (2021).
33. N.-S. Cheng and A. W.-K. Law, *Powder Technol.*, **129**, 156 (2003).
34. A. Barletta, *Int. J. Heat Mass Transfer*, **52**(21), 5266 (2009).
35. R. L. Hamilton and O. Crosser, *Ind. Eng. Chem. Fundam.*, **1**(3), 187 (1962).
36. S. Kumar, S. K. Prasad and J. Banerjee, *Appl. Math. Modell.*, **34**(3), 573 (2010).
37. J. Gong, C. Min, C. Qi, E. Wang and L. Tian, *Int. Commun. Heat Mass Transf*, **43**, 53 (2013).
38. C. Qi, J. Tu, Z. Ding, Y. Wang, L. Sun and C. Wang, *Asia-Pac. J. Chem. Eng.*, **e2668**, 1 (2021).
39. N. Zhao, L. Guo, C. Qi, T Chen and X Cui, *Energy Convers. Manage.*, **181**, 235 (2019).